Three-dimensional vorticity measurements in the wake of a yawed circular cylinder

T. Zhou,[1,a] H. Wang,[2] S. F. Mohd. Razali,[1] Y. Zhou,[3] and L. Cheng[1]
[1]*School of Civil and Resource Engineering, The University of Western Australia, 35 Stirling Highway, Crawley, WA 6009, Australia*
[2]*School of Civil Engineering and Architecture, Central South University, Changsha 410083, China*
[3]*Department of Mechanical Engineering, The Hong Kong Polytechnic University, Hung Hom, Kowloon, Hong Kong*

(Received 28 April 2009; accepted 7 December 2009; published online 15 January 2010)

Using a phase-averaged technique, the dependence of the wake vortical structures on cylinder yaw angle α (=0°–45°) was investigated by measuring all three-velocity and vorticity components simultaneously using an eight-hot wire vorticity probe in the intermediate region ($x/d=10$) of a yawed stationary circular cylinder wake. For all yaw angles, the phase-averaged velocity and vorticity contours display apparent Kármán vortices. It is found that when $\alpha \leq 15°$, the maximum coherent concentrations of the three vorticity components do not change with α. However, when α is increased to 45°, the maximum concentrations of the coherent transverse and spanwise vorticity components decrease by about 33% and 50%, respectively, while that of the streamwise vorticity increases by about 70%, suggesting that the strength of the Kármán vortex shed from the yawed cylinder decreases and the three dimensionality of the flow is enhanced. The maximum coherent concentrations of u and v contours decrease by more than 20% while that of w increases by 100%. Correspondingly, the coherent contributions to the velocity variances $\langle u^2 \rangle$ and $\langle v^2 \rangle$ decrease, while that of $\langle w^2 \rangle$ increases. These results may indicate the generation of the secondary axial vortices in yawed cylinder wakes when α is larger than 15°. The incoherent vorticity contours $\langle \omega_{xr}^2 \rangle$ are stretched along an axis inclining to the x-axis at an angle β in the range of 60°–25° for α =0°–45°. The magnitudes of $\sqrt{\langle \omega_{xr}^2 \rangle}^*$ and $\sqrt{\langle \omega_{yr}^2 \rangle}^*$ through the saddle points are comparable to the maximum concentration of the coherent spanwise vorticity $\tilde{\omega}_z^*$ at all cylinder yaw angles, supporting the previous speculation that the strength of the riblike structures in the cylinder wake is about the same as that of the spanwise structures, even in the yawed cylinder wakes. © *2010 American Institute of Physics*. [doi:10.1063/1.3291072]

I. INTRODUCTION

When a fluid flows over a circular cylinder at a Reynolds number exceeding 47–49,[1–3] a laminar two-dimensional (2D) periodic wake of staggered vortices of opposite sign is formed, where the Reynolds number Re is defined as Re $=U_\infty d/\nu$ with U_∞ being the free-stream velocity in the streamwise direction, d the cylinder diameter, and ν the kinematic viscosity of the fluid. The vortices can be either parallel or oblique to the cylinder axis, depending on the end boundary conditions, which also caused vortex dislocation in the laminar shedding regime.[4] These forms of vortex shedding result in a 20% disparity in the relationship between the Strouhal number and Reynolds number in the laminar shedding regime.[5] When Re is increased to above 180, there exists a transition of the 2D wake to three-dimensional (3D) wake. It is now well known that this transition is associated with two discontinuous changes in the wake formation,[4] which may be manifested by discontinuous changes in the Strouhal number–Reynolds number relationship, or the change in base suction coefficient.[3,6] The first discontinuity, defined as mode A shedding by Williamson,[7] is hysteric and occurs at Re=180–190, depending on the experimental conditions.[2,3,6,8,9] It is associated with the inception of the vortex loops and the formation of the streamwise vortex pairs due to deformation of the primary vortices. The spanwise wavelength of the loops is around $3 \sim 4d$. Using highly accurate numerical methods and Floquet stability analysis, Henderson and Barkley[10] predicted the onset of mode A instability occurring at Re=188.5 with a spanwise wavelength of $4d$, which is very close to the experimental results above.[1–5] The second discontinuity occurs over Re =230–260, defined as mode B shedding,[5] which involves a gradual transfer of energy from mode A to mode B. It is associated with the formation of the riblike small-scale streamwise vortex pairs with a spanwise wavelength of about $1d$.[4] Within the transition, large-scale spotlike vortex dislocations caused by local shedding-phase dislocation along the span of the cylinder have been identified.[7] The above phenomena, namely, vortex dislocation, parallel and oblique shedding, and cellular shedding at low Re, are also observed at high Re turbulent wakes. Prasad and Williamson[11] showed that at Re=5000, parallel and oblique shedding can be triggered by manipulating the cylinder end conditions. Some evidences of vortex dislocation over the span at Re=10 000 were also provided by Norberg.[12] Even at Re=130 000, the

[a]Electronic mail: tzhou@civil.uwa.edu.au.

experimental results for cylinder aspect ratio of 7 by Szepessy and Bearman[13] strongly suggested the existence of vortex dislocation in their wakes. Therefore, Prasad and Williamson[11] suggested that vortex dislocation may be a feature of the flow for Re up to 200 000. When vortices are shed from a cylindrical structure, the latter is subjected to time-dependent drag and lift forces. The forces will result in vibrations if the vortex shedding frequency is close to the natural frequency of the bluff body, which may influence the fatigue life of the structure. As in nearly all the engineering applications such as marine piles and pipelines and braced members of offshore structures, the Reynolds numbers are much larger than the above critical values, turbulent vortex shedding is a widely existing phenomenon.

In some engineering applications, such as flow past cables of a cable-stayed bridge,[14–16] subsea pipelines and marine risers, raker piles on deepwater oil terminals,[17] etc., the incoming flow approaches the cylindrical structures obliquely. In these cases, the fluid velocity in the axial direction of the structure may not be negligible, which may influence the vortex structures and enhance the three dimensionality of the flow downstream. However, the study of yawed cylinder wakes is far less extensive than that of a cylinder in a cross flow. In the present study, the yaw angle (α) is defined as the angle between the free-stream velocity and the plane, which is perpendicular to the cylinder axis, so that $\alpha=0°$ corresponds to the cross-flow case while $\alpha=90°$ corresponds to the axial-flow case. A number of studies have been conducted on the vortex shedding from a stationary yawed cylinder both experimentally (e.g., Refs. 17–22) and numerically (e.g., Refs. 23–26) for yaw angles ranging from 0° to 75°. It was found that the force coefficients and the Strouhal number, when normalized by $U_N(\equiv U_\infty \cos\alpha)$, the velocity component normal to the cylinder axis, are approximately independent of α. This is often known as the independence principle (IP) or the cosine law. One implication of the IP is that the yaw angle does not influence the spanwise coherence of the vortex shedding.[17] There are a number of studies on the validity of the IP. Van Atta[22] showed that for nonvibrating inclined cylinders, the decrease in the vortex shedding frequency followed approximately the IP for $\alpha \leq 35°$, whereas this decrease was slower than that predicted by the IP for larger α. Kozakiewicz *et al.*[19] showed that the IP could be applied to stationary cylinders in the vicinity of a plane wall in the subcritical range, and explained based on the flow visualization results that, although the approaching flow was at an angle to the cylinder (i.e., $\alpha \neq 0°$), the streamlines around the surface of the cylinder were roughly perpendicular to the cylinder axis, providing a validation for the use of the normal velocity component in determining the normalized shedding frequency or the Strouhal number and steady drag. These authors found that the wake characteristics began to change at $\alpha=55°$. They inferred that the IP was valid until $\alpha=55°$. The numerical simulations of Zhao *et al.*[25] verify the IP satisfactorily in terms of Strouhal numbers up to $\alpha=60°$. They also showed that with the increase in α, the vortex shedding angle is less well defined as compared with that in a cross flow and the vortices are distorted. Ramberg[18] studied the effect of the yaw angle up to $\alpha=60°$ and the end conditions on vortex shedding for both stationary and forced vibrating circular cylinders with aspect ratios of 20–90 at Re=160–1100. His results were very sensitive to the end conditions especially at low Reynolds numbers, and the slantwise vortex shedding at an angle other than the cylinder yaw angle was intrinsic to the stationary inclined cylinders in the absence of the end effects, leading to the violation of the IP. Based on numerical simulations, Lucor and Karniadakis[20] found that the angle of vortex shedding from a yawed stationary cylinder was somewhat less than the cylinder's yaw angle, which violated the IP. While the previous studies mostly focused on vortex shedding frequencies, base pressure, and drag and lift forces, there have been no detailed studies on the effect of α on the three dimensionality of the wake flow behind a yawed circular cylinder. This knowledge is of both fundamental and practical importance to our understanding of the physics of vortex shedding, three dimensionality of the velocity and vorticity fields, the change in the coherent structures, and the vortex dislocation in the yawed cylinder wake at subcritical Reynolds numbers. A 3D detached eddy simulation was conducted by Yeo and Jones[26] for three different spanwise aspect ratios ($L/d=10$, 20, and 30, where L and d are the length and diameter of the cylinder, respectively) using both slip wall and periodic wall conditions for the spanwise wall boundary conditions. They found that the slip wall spanwise boundary conditions influenced the vortex flow structures significantly over quite a large spanwise range from the upper end of the cylinder, which was not the case if the periodic spanwise wall boundary conditions were used. It can also be inferred from their isosurface contours of the second invariant that the vortex flow structures downstream of the cylinder were generally parallel to the cylinder except at locations where intense vorticity, low pressure, and swirling flow were found. These locations were not fixed but shifted along the cylinder axis, which was associated with the spanwise velocity component of the flow.

In the present study, the effects of α on the 3D velocity and vorticity fields, the strength of the coherent structures, and the vortex shedding frequency are examined using a 3D vorticity probe, consisting of eight-hot wires at U_∞ of about 8.5 m/s, corresponding to Re=7200. Since vorticity is an important characteristic of turbulence,[27] it would be ideal to measure all three vorticity components simultaneously across the wake. This is, however, impractical due to possible blockage to the flow and the tremendous difficulties involved in dealing with a great number of 3D vorticity probes. Alternatively, a phase-average technique developed by Kiya and Matsumura[28] can be used to study the topology of the coherent and incoherent flow structures in the cylinder wake. This technique has also been used by Zhou *et al.*[29] to investigate the wake of two interfering cylinders. It requires only one moving measurement probe and one fixed single wire or X wire for reference signals, thus providing a good compromise between the sophistication of the vorticity probe and the need to measure the flow field for the study of large-scale vortical structures. The present work provides a relatively complete set of data for the three-velocity and vorticity components at a streamwise location of $x/d=10$ for different

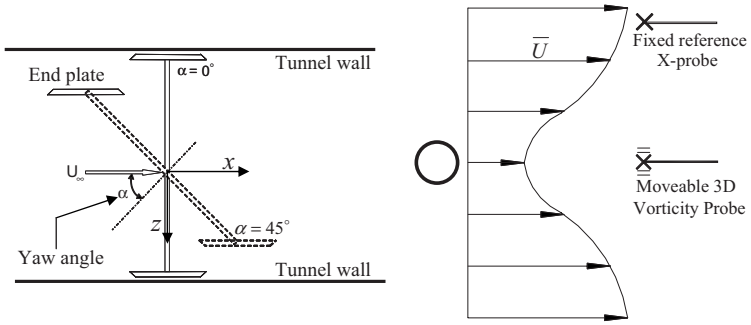

(a) Cylinder arrangement and coordinate system (plan view)

(b) Wake profile and probe arrangements (side view)

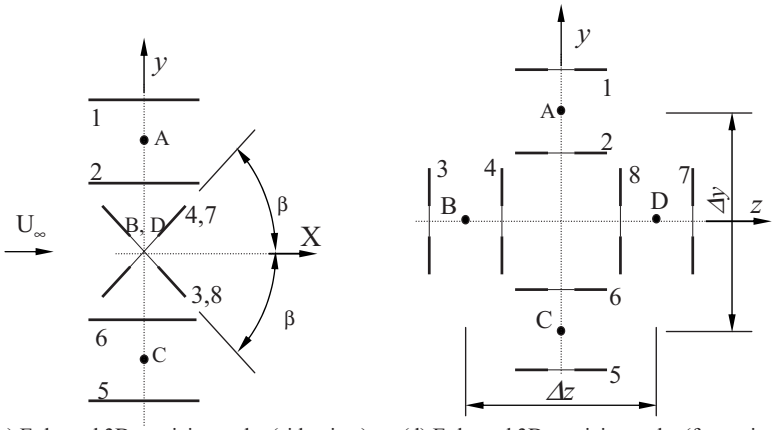

(c) Enlarged 3D vorticity probe (side view)

(d) Enlarged 3D vorticity probe (front view)

FIG. 1. Sketches of the coordinate system and the 3D vorticity probe.

cylinder yaw angles. The analysis of the measurements is conducted by using the phase-average technique to the velocity and vorticity signals to obtain the coherent and incoherent contours and to examine their dependence on cylinder yaw angle. This study also quantified the contributions of the phase-averaged coherent and incoherent structures to the velocity and vorticity components, and based on these results, the effects of the yaw angle α on the wake structures can be examined in details. After an introduction in Sec. I, the experimental setup is given in Sec. II. The velocity and vorticity signals for cylinder yaw angles of 0° and 45° are examined in Sec. III. The phase averaging and structural averaging of the vorticity and Reynolds stresses and their dependence on α are discussed in Secs. IV and V. Based on the above discussion, conclusions are drawn in Sec. VI.

II. EXPERIMENTAL SETUP

The experiments were conducted in a closed loop wind tunnel with a test section of 1.2 m(width)×0.8 m(height) and 2 m long. The free stream across the tunnel is uniform to within 0.5%. The free-stream turbulence intensity is less than 0.5%. All three components of the vorticity vector are measured simultaneously in the cylinder wake at downstream locations $x/d=10$, 20, and 40 for $\alpha=0°$, 15°, 30°, and 45°, respectively. However, due to the limitation of the paper length, only results obtained at $x/d=10$ are shown in the present paper. The results on the evolution of vortex structures in the streamwise direction will be published elsewhere. The cylinder is a 115 cm long smooth stainless steel cylinder with an outer diameter of 12.7 mm. It is aligned horizontally at the center of the test section and supported rigidly at the ends by two square aluminum plates to eliminate the sidewall boundary layer effects. The coordinate system is defined such that the x-axis is in the same direction as the incoming flow. The y-axis is perpendicular to the x-axis in the vertical plane through the cylinder and out of the paper toward the reader, and the z-axis is normal to both x and y axes [Fig. 1(a)]. A vorticity probe was moved across the wake in the y-direction to measure simultaneously the 3D vorticity components. Another X probe located at $y=4-7d$ was used in conjunction with the vorticity probe to provide a phase reference for the measured velocity and vorticity signals [Fig. 1(b)]. The vorticity probe consists of four X probes (i.e., X probes A, B, C, and D), as shown in Figs. 1(c) and 1(d). Two X probes (B and D) aligned in the x-y plane and separated in the z-direction measure velocity fluctuations u and v; the other two (A and C) aligned in the x-z plane and separated in the y-direction measure velocity fluctuations u and w. The separations between the centers of the two opposite X probes (either B and D or A and C) were about 2.7 mm. The separation between the two inclined wires of each X probe was about 0.7 mm. The hot wires were etched from Wollaston (Pt-10% Rh) wires. The active length was about $200d_w$, where $d_w(\equiv 2.5\ \mu\text{m})$ is the wire diameter. The angle calibration was performed over ±20°. The included angle of each X probe was about 110° and the effective angle of the inclined wires was about 35°. The signals were low pass filtered at a frequency of 5200 Hz and subsequently sampled

at a frequency $f_s=10\,400$ Hz using a 16 bit analog-to-digital converter. The record duration T_s was about 20 s. As in the present study, the measured minimum vortex shedding frequency at $\alpha=45°$ is 102 Hz. This record duration corresponds to 2040 cycles, which is about 14 times of the suggested signal length[30] for studying the vortex shedding. The number of independent samples $N \equiv T_s/2T_u$ suggested by Tennekes and Lumley[27] is around 12 320, where $T_u \equiv \int_0^{\tau_0} \rho_{uu}(\tau)d\tau$ is an integral time scale, ρ_{uu} is the longitudinal velocity autocorrelation coefficient of u, and τ_0 is the time at which the first zero crossing occurs.

The vorticity components are calculated from the measured velocity signals, viz.,

$$\omega_x = \frac{\partial w}{\partial y} - \frac{\partial v}{\partial z} \approx \frac{\Delta w}{\Delta y} - \frac{\Delta v}{\Delta z}, \tag{1}$$

$$\omega_y = \frac{\partial u}{\partial z} - \frac{\partial w}{\partial x} \approx \frac{\Delta u}{\Delta z} - \frac{\Delta w}{\Delta x}, \tag{2}$$

$$\omega_z = \frac{\partial v}{\partial x} - \frac{\partial (\bar{U}+u)}{\partial y} = \frac{\Delta v}{\Delta x} - \frac{\Delta (\bar{U}+u)}{\Delta y}, \tag{3}$$

where Δw and Δu in Eqs. (1) and (3), respectively, are the velocity differences between X probes A and C; Δv and Δu in Eqs. (1) and (2), respectively, are the velocity differences between X probes B and D. The velocity gradients in the streamwise direction $\Delta w/\Delta x$ and $\Delta v/\Delta x$ are obtained by using a central difference scheme to the time series of the measured velocity signals, e.g., $\Delta v/\Delta x \approx [v(i+1)-v(i-1)]/\Delta x$, where the streamwise separation Δx is estimated based on Taylor's hypothesis given by $\Delta x = -U_c(2\Delta t)$, as U_c is the convection velocity of vortices and Δt $(\equiv 1/f_s)$ is the time interval between two consecutive points in the time series of the velocity signals. A central difference scheme in estimating $\Delta w/\Delta x$ and $\Delta v/\Delta x$ would have the advantage to avoid phase shifts between the velocity gradients involved in Eqs. (2) and (3).[31]

Experimental uncertainties in $\bar{U}$ and u' (or v' and w') were inferred from the errors in the hot-wire calibration data as well as the scatter (from 20 to 1 odds) observed in repeating the experiment for a number of times. Hereafter, a superscript prime denotes the root-mean-square (rms) values. The uncertainty for U was about $\pm 4\%$, while the uncertainties for u', v', and w' were about $\pm 7\%$, $\pm 8\%$, and $\pm 8\%$, respectively. The uncertainty for wire separation Δx was about $\pm 4\%$ and that for Δy or Δz was about $\pm 5\%$. Using these values, the uncertainties for vorticity components were estimated by the method of propagation of errors (e.g., Refs. 32–34). The resulting maximum uncertainties for ω_x, ω_y, and ω_z were about $\pm 14\%$, $\pm 13\%$, and $\pm 13\%$, respectively. It needs to be noted that these estimations of uncertainties do not include the spectral attenuation caused by the unsatisfactory spatial resolution in Δx, Δy, and Δz of the 3D vorticity probe.[35] The correction of the spectral attenuation is based on the assumption of isotropy of the flow. Unfortunately, the spectral attenuation effect cannot be corrected in the present study due to the lack of isotropy at $x/d=10$ for the shedding of large organized vortex structures. The vortex shedding frequency is identified using the fast Fourier transform algorithm with a window size of 2.[11] The frequency resolution on the power spectra is about 2.5 Hz. Taking into the uncertainties in hot wire calibration, incoming velocity measurements and misalignment, etc., the uncertainty in the Strouhal number (will be defined later) is conservatively estimated to be not more than 8%.

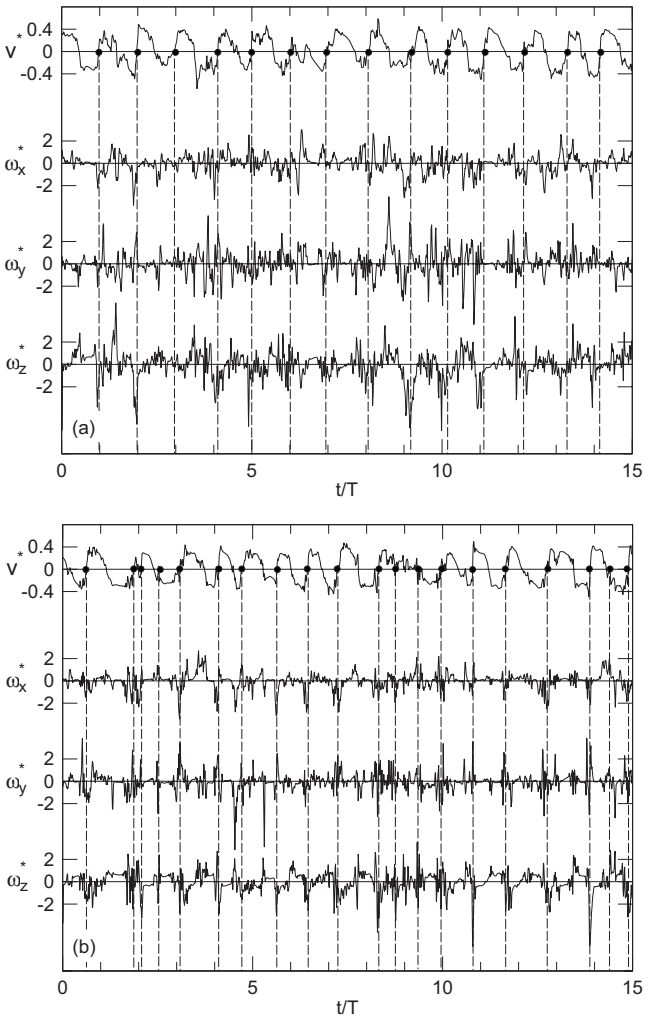

FIG. 2. Time traces of the fluctuating transverse velocity v and the three vorticity components measured at $y/d=0.5$. The dots on the traces of the v signals indicate the possible centers of the spanwise vortices. (a) $\alpha=0°$; (b) $\alpha=45°$.

III. VELOCITY AND VORTICITY SIGNALS

Figure 2 shows the time traces of the fluctuating velocity v measured at $y/d=0.5$ for $\alpha=0°$ and 45°, respectively, together with signals for ω_x, ω_y, and ω_z. In the figure, an asterisk denotes normalization by d and U_∞. Previous studies have shown that $y/d=0.5$ is the location of the vortex centers.[29] The v-signals at both yaw angles show apparent large-scale quasiperiodical fluctuations with relatively fixed frequency, indicating the occurrence of the Kármán vortices. The fluctuation of the velocity signals is not as significant as the vorticity signals. This result clearly shows that the vorticity signals represent more small-scale structures. As indicated by the dashed vertical lines, there is in general a cor-

TABLE I. Flatness factors of the vorticity components at $\alpha=0°$ and 45°.

α (deg)	F_{ω_i}		
	ω_x	ω_y	ω_z
0	5.83	6.6	6.02
45	7.46	8.94	6.24

respondence between the large negative ω_z fluctuations and zero-crossing point (positive dv/dt) of the v-signal. Based on conditional analysis results, Zhou and Antonia[36] found a correspondence between the center of spanwise vortices (negative sign) and zero v of positive dv/dt. Therefore, the zero values of v at positive dv/dt, marked by dots in the v-signals (Fig. 2), are identified with the possible Kármán vortex center. Similarly, the ω_x and ω_y signals also exhibit considerable fluctuations at the vortex centers, although at relatively small scales in terms of timewise or longitudinal spatial distance, reflecting the three dimensionality of the Kármán vortices. At $\alpha=0°$, the fluctuations of the vorticity signals are quite significant. However, at $\alpha=45°$, all the three vorticity signals show apparent enhanced intermittency which can be reflected by the flatness factors $F_{\omega_i}(\equiv\langle\omega_i^4\rangle/\langle\omega_i^2\rangle^2)$ of the vorticity components. The values of F_{ω_i} for the two angles are given in Table I. This result indicates that the shedding of vortices at high yaw angles is not as strong as that in a cross flow ($\alpha=0°$). We have checked that with the increase in α from 0° to 45°, the change in vorticity signals is gradual. Zhao *et al.*[25] and also Lucor and Karniadakis[20] showed that as α is increased, the shape of the vortices is distorted, and locally the axial vortices may or may not be parallel to the cylinder axis. It is also found by these authors that the vortices right behind the cylinder are convected not only in the incoming flow direction, but also in the cylinder axial direction, which is consistent with that of Yeo and Jones.[26] The enhanced spanwise velocity as α is increased helps to dislocate the large-scale structures and enhance the three dimensionality of the flow, resulting in dispersion of the large-scale vortical structures. This result may indicate that with the increase in α, the intermittency of the vortex structures increases, which can be revealed also by the probability density function (pdf) of the vorticity signals.

The pdfs of the three vorticity components for $\alpha=0°$ and 45° are shown in Fig. 3. Also shown in the figure is the Gaussian distribution. The pdf is defined such that $\int_{-\infty}^{\infty}P_{\omega_i}d\omega_i=1$. The measured distributions of the vorticity pdf are apparently nonsymmetric. They exceed the Gaussian distribution for both large and small amplitude fluctuations. The distributions of P_{ω_x} and P_{ω_y} show a pronounced peak at around zero. It can be seen that for small vorticity fluctuations, with the increase in α, the shapes of the pdfs of ω_x and ω_y contracted and their amplitudes increased. For large vorticity fluctuations, the tails of both P_{ω_x} and P_{ω_y} spread out slightly and follow a single exponential distribution as α is increased from 0° to 45°, indicating an increased F_{ω_y} and F_{ω_z}. The distribution of P_{ω_z} exhibits twin peaks [Fig. 3(c)]. The peak of negative vorticity is due to the spanwise vortices

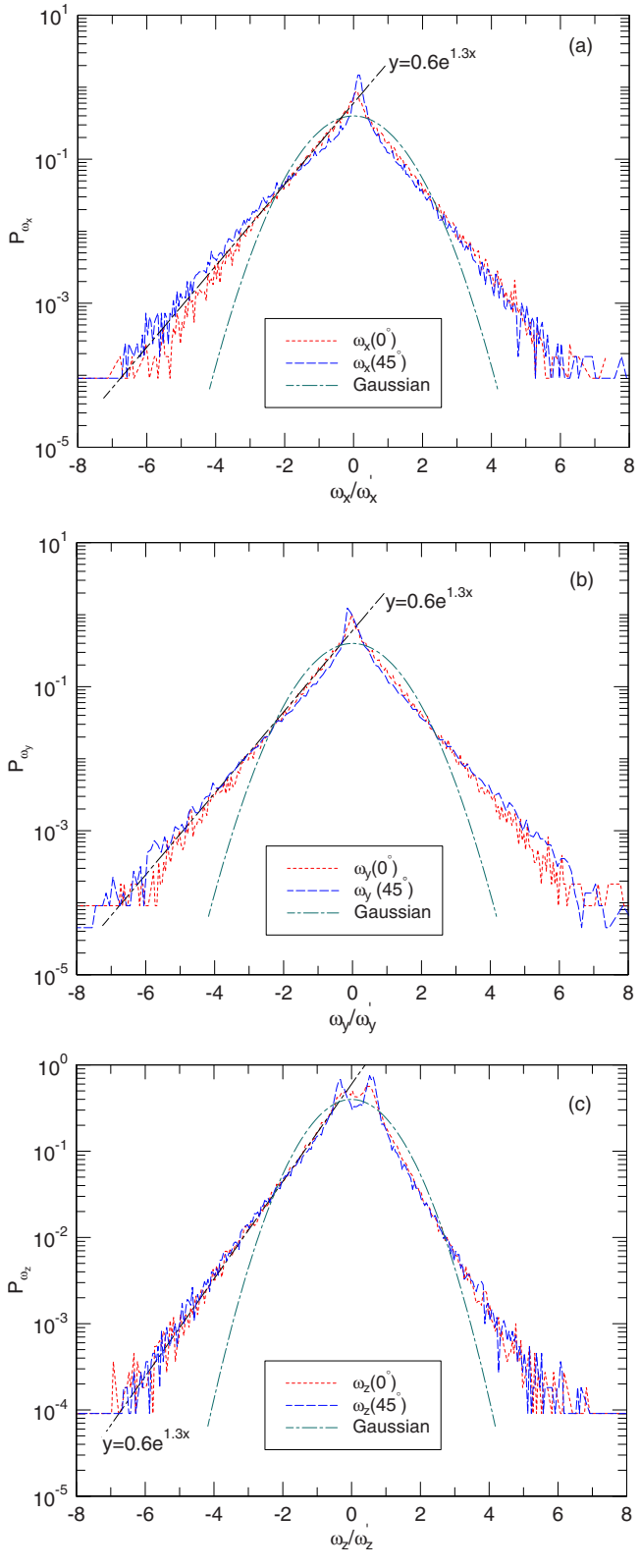

FIG. 3. (Color online) pdf of vorticity components at $\alpha=0°$ and 45°. (a) ω_x; (b) ω_y; (c) ω_z.

of negative sign that occurs at $y/d>0$, whereas that of positive vorticity is attributed to the spanwise vortices of positive sign, whose center is at $y/d<0$. As α is increased from 0° to 45°, the twin peaks in P_{ω_z} increase slightly and shift to larger values of ω_z/ω_z', while the magnitude of P_{ω_z} around zero

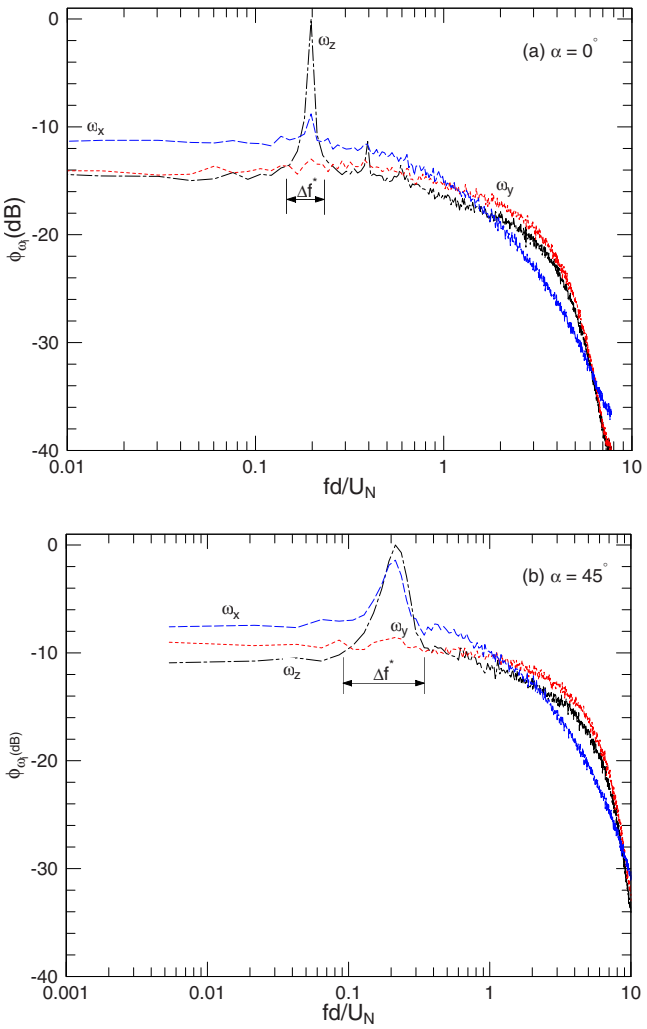

FIG. 4. (Color online) Spectra of three vorticity components at (a) $\alpha=0°$ and (b) $\alpha=45°$.

also increases. For $\alpha=0°$, an expression $P_{\omega_i} \sim e^{\gamma x}$ fits the exponential tail adequately (where $\gamma=1.3$ and x stands for the negative vorticity fluctuations normalized by the rms values), which is close to that reported by Kida and Murakami[37] using direct numerical simulations, where a power of $\sqrt{2}$ was reported. When α is increased to 45°, the slope of the tails for P_{ω_x} and P_{ω_y} decreases slightly even though it still shows a single exponential distribution. The slightly increased peaks for all the three vorticity components in the vicinity of the origin indicate the increased flatness factors with the increase in the yaw angle, which is consistent with the results shown in Fig. 2.

Figure 4 shows the vorticity spectra ϕ_{ω_x}, ϕ_{ω_y}, and ϕ_{ω_z}, measured at the wake vortex center $(y/d=0.5)$ for $\alpha=0°$ and 45°, respectively. The vorticity spectrum ϕ_{ω_i} has been normalized to the decibel scale using the maxima of ϕ_{ω_z} at $\alpha=0°$ and 45°, respectively, while the frequency is normalized by U_N and d, i.e., $x=fd/U_N$ and $U_N(\equiv U_\infty \cos\alpha)$ is the velocity component normal to the cylinder axis. With this normalization, the peak frequency f_0 on the spectrum, or after normalization, $f_0 d/U_N$, corresponds to the Strouhal number St_N $(\equiv f_0 d/U_N)$. For all cases, there is a clear peak on the vorticity spectra, which corresponds to the Strouhal number. For $\alpha=0°$, $\mathrm{St}_0=0.195$, which is the same as our previous results.[38,39] The peak on the spectrum ϕ_{ω_z} is sharp and narrow, which occurs over a narrow range (Δf^*) of $f^*=0.146-0.223$. There is only a minor peak on ϕ_{ω_x}. The peak heights relative to the heights of the plateaux on the vorticity spectra ϕ_{ω_x} and ϕ_{ω_z} over the range of $f^*=0.004-0.12$ are 2.6 and 14 dB, respectively. When α is increased to 45°, the peak on the spectrum ϕ_{ω_z} is much less sharp and the peak region (Δf^*) is enlarged to $f^*=0.090-0.34$. In contrast to $\alpha=0°$, the peak on ϕ_{ω_x} is increased and becomes more apparent, even though the peak region is enlarged. The peak heights relative to the heights of the plateaux on the vorticity spectra ϕ_{ω_x} and ϕ_{ω_z} over the range of $f^*=0.004-0.1$ are 6 and 10.6 dB, respectively, indicating a reduced spanwise vortex shedding intensity and an enhanced streamwise vortex shedding intensity. These results indicate the dispersion of the turbulent energy over the vortex shedding frequency, as well as the enhancement of the three dimensionality of the flow. Williamson[4] stated that after the onset of the turbulent shedding and with the increase in Reynolds number, there seems to be an increased disorder in the fine-scale three dimensionality associated with the secondary and essentiality streamwise-oriented vortices of type mode B. The study of Mansy *et al.*[40] showed that the increase in the secondary or streamwise vortices probably is at the expense of the primary spanwise vortices, which is consistent with the trend shown in Fig. 4. The present results are also consistent with the vorticity isocontours obtained by Lucor and Karniadakis[20] and Zhao *et al.*,[25] who showed that as α is increased, the shape of the spanwise vortices is distorted and reveals a helical style. The large-scale organized structures found in the wake of a cross flow are broken down and the vortex shedding angle of the spanwise vortices is much less well defined. They may or may not be parallel to the cylinder axis. It is also found that vortices right behind the cylinder are convected not only in the incoming flow direction, but also in the cylinder axial direction. This results in the dispersion of the large-organized vortical structures. The peak frequencies on the spectra of ϕ_{ω_i} suggest that with the increase in α, the Strouhal number St_N changes gradually from 0.195 at $\alpha=0°$ to 0.202, 0.206, and 0.224 for $\alpha=15°$, 30°, and 45°, respectively, increasing monotonically with α (figures for $\alpha=15°$ and 30° are not shown here). However, as the St_N values at $\alpha=15°$ and 30° are only about 4% and 6% higher than that obtained at $\alpha=0°$, these differences may be disguised by the experimental uncertainty of St_N, which is estimated to be not more than ±8%, and St_N can be considered as a constant. The increase in St_N from $\alpha=0°$ to 45° (by about 15%) cannot be ascribed to the experimental uncertainty. It may reflect a genuine departure from the IP for large α. In this case, significant mean spanwise velocity component $\bar{W}$ has been measured as α is increased,[39] which was conjectured as the main mechanism by which the axial velocity might act to destabilize the vortex street and cause the vortex dislocation in the spanwise direction, leading to the breakdown of the IP for sufficiently large yaw angles.[23]

The spanwise velocity $\bar{W}$ provides a measure of three

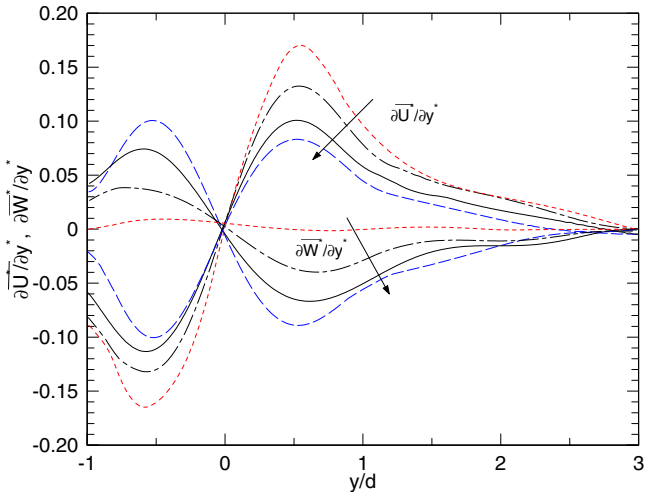

FIG. 5. (Color online) Normalized velocity gradients for different α at $x/d=10$. The arrows indicate the direction of increasing α. ---: $\alpha=0°$; — - —: 15°; ——: 30°; — —: 45°.

dimensionality of the flow.[14] A larger magnitude in $\bar{W}$ implies a higher degree of three dimensionality and a stronger instability of the vortex filament.[13] The variations in $\partial\bar{W}/\partial y$ at $x/d=10$ for different α are shown in Fig. 5. The values of $\partial\bar{W}/\partial y$ for $\alpha=0°$ are close to zero, consistent with the quasi-two-dimensionality of the flow. This result also implies that the vortex shedding is parallel with the cylinder axis.[41] Clearly, with the increase in α, the magnitude of $\partial\bar{W}/\partial y$ increases. The maximum mean velocity gradient $\partial\bar{W}/\partial y$ occurs at around $y/d=0.5-0.65$, depending on α; with the increase in α, the location of the maximum mean shear $\partial\bar{W}/\partial y$ approaches to the centerline. This result implies an increased mean streamwise vorticity $\bar{\omega}_x(\equiv\partial\bar{V}/\partial z-\partial\bar{W}/\partial y)$ as α is increased. For comparison, the distributions of $\partial\bar{U}/\partial y$ at $x/d=10$ for different α are also included in the figure. The magnitude of $\partial\bar{U}/\partial y$ is comparable to that of $\partial\bar{W}/\partial y$ at large yaw angles. Its values decrease with the increase in α, indicating a decreased mean spanwise vorticity $\bar{\omega}_z(\equiv\partial\bar{V}/\partial x-\partial\bar{U}/\partial y)$ with the increase in α. Due to the small magnitude of $\bar{V}$ and hence the small velocity gradients of $\bar{V}$ in the x- and z-directions, the magnitudes of $\partial\bar{V}/\partial x$ and $\partial\bar{V}/\partial z$ in the expressions of $\bar{\omega}_z$ and $\bar{\omega}_x$ [Eqs. (2) and (3)] should be negligible and the spanwise mean vorticity $\bar{\omega}_z$ is comparable in magnitude to the streamwise mean vorticity $\bar{\omega}_x$.

The present measurements allow the shedding angle downstream of the cylinder to be evaluated using the method proposed by Hammache and Gharib.[41] They showed that for oblique shedding, the shedding angle θ is related with the vorticity components $\bar{\omega}_x$ and $\bar{\omega}_z$, viz.,

$$\tan\theta=\bar{\omega}_x/\bar{\omega}_z, \tag{4}$$

which can then be simplified further as

$$\tan\theta=S_W/S_U, \tag{5}$$

where S_W and S_U are the maximum velocity gradients on the distributions of $\partial\bar{W}/\partial y$ and $\partial\bar{U}/\partial y$. The shedding angle $\theta[\equiv\tan^{-1}(S_W/S_U)]$ at different cylinder yaw angle α can then be calculated from the values of S_W and S_U (Fig. 5). The shedding angles θ for different cylinder yaw angles are listed in Table II. The values of θ agree very well with the corresponding cylinder yaw angle α, indicating that the vortex is parallel to the cylinder in the present study.

Autocorrelation coefficient can be used to highlight the differences of the organized structures at different yaw angles. The autocorrelation coefficient is defined as $\rho_\beta=\langle\beta(x)\beta(x+r)\rangle/\langle\beta^2\rangle$, where β represents the vorticity components ω_x, ω_y, and ω_z, and r is the longitudinal separation between the two points, which is calculated using Taylor's hypothesis by converting the time delay τ to a streamwise separation via $r=\tau U_N/f_s$. The autocorrelation coefficients for ω_x, ω_y, and ω_z at different cylinder yaw angles are shown in Fig. 6. For $\alpha\leq15°$, the autocorrelation coefficient ρ_{ω_x} is very small and there is nearly no periodicity. When α is increased to 30°, ρ_{ω_x} starts to reveal some periodicity, especially at 45°. This result is consistent with the increase in $\bar{W}$ as α increases, since the increase in $\bar{W}$ causes the instability of the primary vortex shedding, leading to the enhancement of the three dimensionality of the wake.[13] The distributions of ρ_{ω_y} show no periodicity at all α. This is consistent with the spectrum of ω_y (Fig. 4), where no peak on ϕ_{ω_y} is identified. The periodicity on the distribution of ρ_{ω_z} is very apparent. This is true as ω_z mainly represents the primary vortices. At $\alpha=0°$, ρ_{ω_z} persists for a long distance. Even at $tU_\infty/d=200$, the periodicity on ρ_{ω_z} is still very apparent. However, with the increase in α, the magnitude of ρ_{ω_z} decreases and approaches zero at a faster rate. For example, at $\alpha=15°$, ρ_u approaches zero at about $tU_\infty/d=60$. This has been decreased to 40 and 14 for $\alpha=30°$ and 45°, respectively. This result indicates that the vortices shed from a yawed circular cylinder decay more rapidly as compared with that at $\alpha=0°$, and the decay is

TABLE II. The vortex shedding angle θ, vortex shedding frequency f_0, convection velocity U_c, wavelength λ, and the inclination angle β between the main vortex stretching direction and the x-axis for different cylinder yaw angles α.

α (deg)	θ (deg)	f_0 (Hz)	U_c/U_∞	λ/d	λ/d (cos α)	β (deg)
0	0.53	132	0.82	4.16	4.16	60
15	16.8	131.2	0.83	4.23	4.09	57
30	33	121.7	0.87	4.8	4.16	45
45	45.6	101.6	0.89	5.86	4.14	25

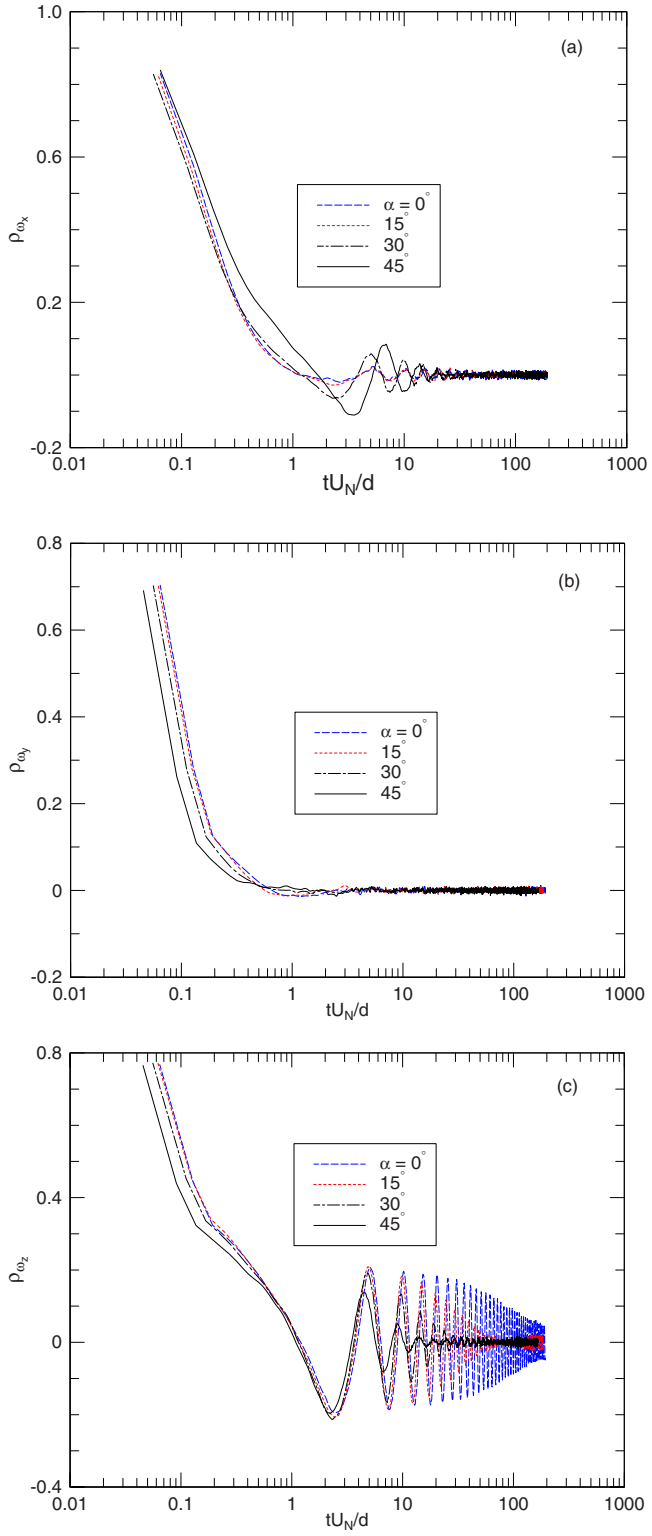

FIG. 6. (Color online) Autocorrelation coefficient ρ_{ω_i} for different α. (a) ρ_{ω_x}; (b) ρ_{ω_y}; (c) ρ_{ω_z}. — —: α=0°; ---: 15°; — - —: 30°; ——: 45°.

more apparent with the increase in α. Comparing with Fig. 6(a), where ρ_{ω_x} increases with α, it seems that the increase in the secondary or streamwise vortices, reflected by ω_x, is at the expense of the primary spanwise vortices, reflected by ω_z, which is in agreement with Mansy *et al.*[40]

IV. PHASE-AVERAGED VELOCITY AND VORTICITY FIELDS

A. Phase averaging

The phase-averaging method is similar to that used by Kiya and Matsumura[28] and Zhou *et al.*[29] Briefly, the v-signal measured by the reference X probe was band pass filtered with the central frequency set at f_0. The two phases of particular interest were identified on the filtered signal v_f, viz.,

$$\text{Phase A:} \quad v_f = 0 \quad \text{and} \quad \frac{dv_f}{dt} > 0, \tag{6}$$

$$\text{Phase B:} \quad v_f = 0 \quad \text{and} \quad \frac{dv_f}{dt} < 0. \tag{7}$$

The two phases correspond to time $t_{A,i}$ and $t_{B,i}$ (measured from an arbitrary time origin), respectively. The phase ϕ was then calculated from v_f, viz.,

$$\phi = \pi \frac{t - t_{A,i}}{t_{B,i} - t_{A,i}}, \quad t_{A,i} \le t \le t_{B,i}, \tag{8}$$

$$\phi = \pi \frac{t - t_{B,i}}{t_{A,i+1} - t_{B,i}} + \pi, \quad t_{B,i} < t \le t_{A,i+1}. \tag{9}$$

The interval between phases A and B was made equal to $0.5/f_0$ by compression or stretching, which was further divided into 30 equal intervals. The difference between the local phase at each y-location of the vorticity probe and the reference phase of the fixed X wire was used to produce phase-averaged sectional streamlines and contours of the coherent vorticities in the (ϕ, y)-plane.

The phase average of an instantaneous quantity B is given by

$$\langle B \rangle_j = \frac{1}{N} \sum_{i=1}^{N} B_{j,i}, \tag{10}$$

where N is the number detected and j represents the phase. For convenience, the subscript j will be omitted hereinafter.

The variable B can be written as the sum of a time-averaged component $\bar{B}$, a coherent fluctuation $\tilde{\beta}$, and a remainder β_r,[42] viz.,

$$B = \bar{B} + \tilde{\beta} + \beta_r, \tag{11}$$

where B stands for instantaneous vorticity or velocity signals and the fluctuation β is given by

$$\beta = \tilde{\beta} + \beta_r. \tag{12}$$

The coherent fluctuation $\tilde{\beta}$ ($\equiv \langle \beta \rangle$) reflects the effect from the large-scale coherent structures while the remainder β_r mainly refers to the incoherent structures. The following equation may be derived from Eq. (12):

$$\langle \beta^2 \rangle = \tilde{\beta}^2 + \langle \beta_r^2 \rangle. \tag{13}$$

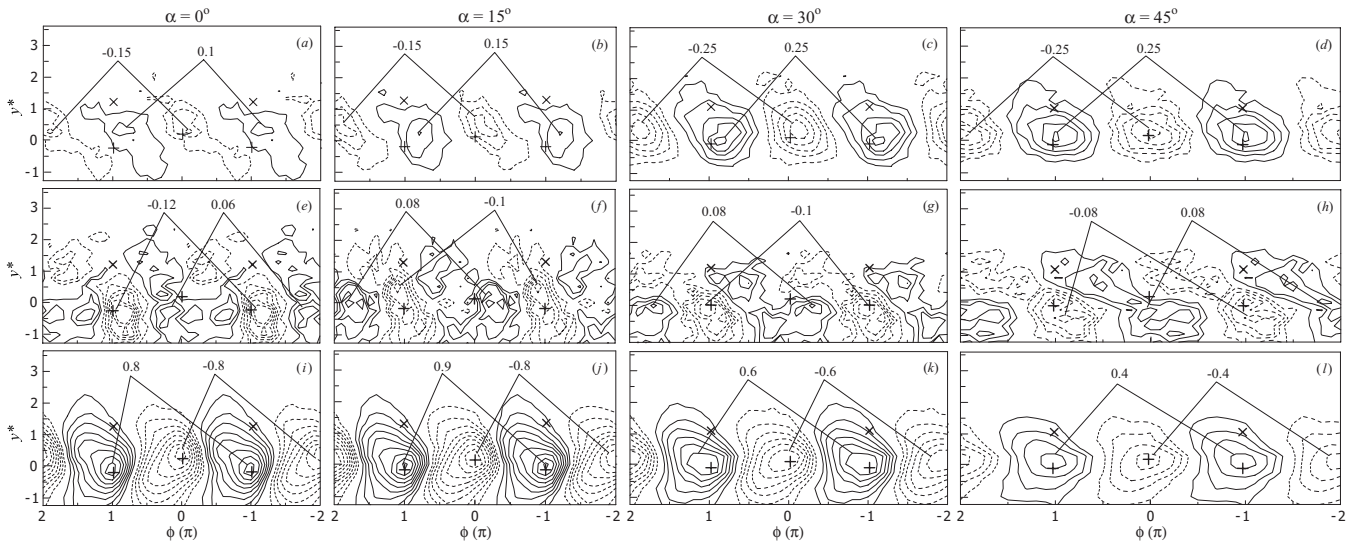

FIG. 7. Phase-averaged coherent vorticity contours at different α. [(a)–(d)] $\tilde{\omega}_x^*$; [(e)–(h)] $\tilde{\omega}_y^*$; [(i)–(l)] $\tilde{\omega}_z^*$. Center and saddle points are marked by plus and cross, respectively. [(a)–(d)] Contour interval=0.05; [(e)–(h)] 0.02; [(i)–(l)] 0.1.

B. Structural averaging

Once the coherent components of velocity and vorticity are extracted, the coherent contributions to the vorticity variances can be obtained in terms of the structural average. For each wavelength, the phase-averaged structure begins at j_1 samples (corresponding to $\phi=-\pi$) before $\phi=0$ and ends at j_2 samples (corresponding to $\phi=\pi$) after $\phi=0$. The structural average, denoted by a double overbar, is defined by

$$\overline{\overline{\tilde{\beta}^2}} = \frac{1}{j_1+j_2+1}\sum_{-j_1}^{j_2}\tilde{\beta}^2. \tag{14}$$

The value for $j_1(=j_2)$ is 24 so that the value (j_1+j_2+1) corresponds approximately to the average vortex shedding frequency. The structurally averaged quantities can provide a measurement of the contribution from the coherent structures to the vorticity variances. Similarly, Eq. (14) may also be used to calculate the contribution of $\langle\overline{\overline{\beta_r^2}}\rangle$, the incoherent structures make to the vorticity variances. The structural average $\langle\overline{\overline{\beta^2}}\rangle$ of the vorticity variances may be derived from Eqs. (13) and (14), viz.,

$$\langle\overline{\overline{\beta^2}}\rangle = \overline{\overline{\tilde{\beta}^2}} + \langle\overline{\overline{\beta_r^2}}\rangle. \tag{15}$$

It has been verified that the difference between $\langle\overline{\overline{\beta^2}}\rangle$ and $\overline{\beta^2}$ in general is within 5%, suggesting that for vorticity, the selected data for phase averaging/structural averaging are representative to the flow.

C. Coherent vorticity fields

Figure 7 presents the isocontours of the phase-averaged or coherent vorticity $\tilde{\omega}_x^*, \tilde{\omega}_y^*$ and $\tilde{\omega}_z^*$ for different yaw angles. The phase ϕ, ranging from -2π to $+2\pi$, can be interpreted in terms of a longitudinal distance; $\phi=2\pi$ corresponds to the average vortex wavelength $\lambda(\equiv U_c/f_0)$, which is given in Table II for different cylinder yaw angles. The values of U_c for different cylinder yaw angles are estimated with the values of $\bar{U}+\tilde{u}$ at the vortex centers. These values are also included in Table II. At $\alpha=0°$, the wavelength of the spanwise vortices is about $4.2d$, in agreement with that found previously.[38] With the increase in cylinder yaw angle, the wavelength increases systematically. However, if a factor of $\cos(\alpha)$ is multiplied with λ, the value $\lambda(\cos\alpha)$ is approximately constant for different angles. This result indicates that the spanwise vortices shed from the yawed cylinder are parallel to the cylinder axis, which is consistent with the shedding angle θ obtained using Eq. (5) (Table II). In Fig. 7 and other figures for isocontours that follow, to avoid any distortion of the physical space, the same scales are used in the ϕ- and y^*-directions. The $\tilde{\omega}_z^*$ contours [Figs. 7(i)–7(l)] display the well known Kármán vortex street for all yaw angles. The vortex centers, identified by the maximum concentration of $\tilde{\omega}_z^*$, coincide well with the foci (marked by + in the figure) determined from the phase-averaged sectional streamlines shown in Fig. 8, which were constructed based on the velocity signals measured by one of the two X wires aligned in the x-y plane. The saddle points determined from the sectional streamlines are marked by ×. The spanwise vortices shrink slowly with the increase in α, changing from $y/d=0.4$ at $\alpha=0°$ to $y/d=0.2$ at $\alpha=45°$ [Figs. 7(i) and 7(l)], indicating a reduced wake region. These results agree well with those reported previously.[20] The maximum concentration of $\tilde{\omega}_z^*$ at $\alpha=0°$ is -0.8 (the negative value of the vorticity contours represents the vorticity above the centerline). This value is slightly lower than that reported previously at a comparable Reynolds number[38] due mainly to the difference in spatial resolution of the probes between the two studies. For $\alpha \leq 15°$, the maximum concentration of $\tilde{\omega}_z^*$ does not change. When α is increased further, the maximum concentration of $\tilde{\omega}_z^*$ decreases. The maximum concentration of $\tilde{\omega}_z^*$ at $\alpha=45°$ decreases by about 50% compared with that at $\alpha=0°$. This result indicates that with the increase in the yaw angle, the spanwise vortex strength decreases, which is in agreement with that shown in Fig. 4.

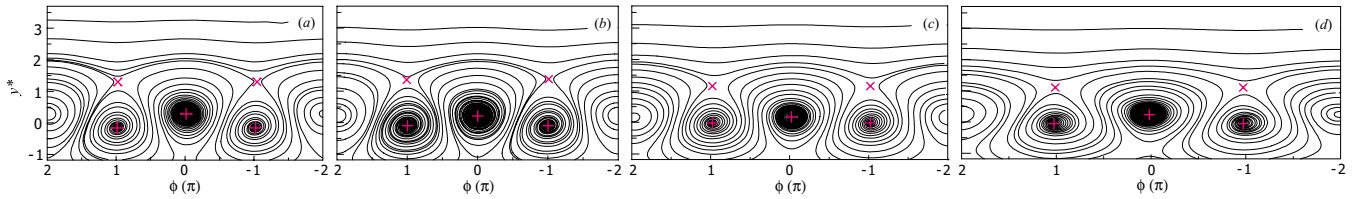

FIG. 8. (Color online) Phase-averaged sectional streamlines at different α. Center and saddle points are marked by plus and cross, respectively. (a) $\alpha=0°$; (b) $\alpha=15°$; (c) $\alpha=30°$; (d) $\alpha=45°$.

The $\tilde{\omega}_x^*$ contours [Figs. 7(a)–7(d)] are much weaker than those of $\tilde{\omega}_z^*$ even though they also exhibit organized patterns, especially at large yaw angles. The size of the longitudinal vortices is much smaller than that of the spanwise structures. The strength of $\tilde{\omega}_x^*$ for $\alpha=0°$ at the vortex center is only about 1/5 of that of $\tilde{\omega}_z^*$. The maximum longitudinal vortex concentrations are shifted away from the Kármán vortex centers. The change in $\tilde{\omega}_x^*$ for $\alpha \leq 15°$ is not apparent. When α is further increased to 30°, the contours of the longitudinal vortices become more organized and the maximum longitudinal vorticity concentration increases by about 70%. This result indicates the generation of the secondary axial vortices or the occurrence of vortex dislocation[4] and an enhanced three dimensionality with the increase in α. As the calculation of ω_x is related with the velocity signal for w, the increase in $\tilde{\omega}_x^*$ should be caused by the increase in w at large yaw angles (see Fig. 10). The $\tilde{\omega}_y^*$ contours at $\alpha=0°$ [Fig. 7(e)] are comparable to that of $\tilde{\omega}_x^*$. With the increase in α, the organized patterns of the $\tilde{\omega}_y^*$ contours become less apparent and the maximum concentration of $\tilde{\omega}_y^*$ decreases consistently. The reduction in $\tilde{\omega}_y^*$ at $\alpha=45°$ is comparable to that of $\tilde{\omega}_z^*$, which is about 33% compared with that at $\alpha=0°$. Overall, from the contours of $\tilde{\omega}_x^*$ and $\tilde{\omega}_z^*$, it can be seen that with the increase in α, the strength of the former increases while it decreases for the latter. At $\alpha=45°$, the magnitudes of the coherent vorticity components $\tilde{\omega}_x^*$ and $\tilde{\omega}_z^*$ tend to be comparable, which are about $-0.25 \sim -0.4$. This result further confirms that with the increase in α, the three dimensionality of a yawed cylinder wake tends to be enhanced, consistent with that shown by Zhou *et al.*[39] This result is also consistent with that of Mansy *et al.*[40] who argued that the increase in the streamwise circulations occurs probably at the expense of the primary spanwise vortex circulation. The maximum contour values of the coherent vorticity for different α are summarized in Table III.

D. Incoherent vorticity fields

Figure 9 shows the incoherent vorticity contours $\langle\omega_{xr}^2\rangle^*$, $\langle\omega_{yr}^2\rangle^*$, and $\langle\omega_{zr}^2\rangle^*$ for different yaw angles. The magnitudes of the maximum incoherent vorticity concentrations at $\alpha=0°$ agree well with our previous published results.[38] They occur at approximately the same location, which is slightly downstream of the vortex centers for all cylinder yaw angles. Note that the $\langle\omega_{xr}^2\rangle^*$ contours running along the diverging separatrix through the saddle point (marked in the figure by $\times$) wrap around the consecutive spanwise structures of opposite sign. Presumably, these contours represent the signature of the streamwise or riblike structures of the wake. It seems that the incoherent vorticity contours $\langle\omega_{xr}^2\rangle^*$ are stretched along an axis which inclines to the x-axis at an angle β in the range between 60° (when $\alpha=0°$) and 25° (when $\alpha=45°$) (shown in Table II). The magnitude of the maximum incoherent vorticity concentration decreases with the increase in α. At $\alpha=0°$, the $\langle\omega_{xr}^2\rangle^*$ contour level through the saddle point is about 0.62, corresponding to a magnitude of $\sqrt{\langle\omega_{xr}^2\rangle^*} \approx 0.79$, which is the same as the maximum magnitude of the coherent spanwise vorticity component $\tilde{\omega}_z^*$ [Fig. 7(i)]. With the increase in α, the $\langle\omega_{xr}^2\rangle^*$ contour level through the saddle point decreases. However, as the spanwise coherent vorticity $\tilde{\omega}_z^*$ decays faster, the magnitude of $\sqrt{\langle\omega_{xr}^2\rangle^*}$ exceeds $\tilde{\omega}_z^*$ for $\alpha > 15°$. The values of $\sqrt{\langle\omega_{xr}^2\rangle^*}$ through the saddle points for different α are compared with the maximum concentration of $\tilde{\omega}_z^*$ in Table III. Also given are the values of $\sqrt{\langle\omega_{yr}^2\rangle^*}$ through the saddle points. It can be seen that the magnitudes of $\sqrt{\langle\omega_{xr}^2\rangle^*}$ and $\sqrt{\langle\omega_{yr}^2\rangle^*}$ exceed the spanwise coherent vorticity at large yaw angles. These results seem to support the speculation of Hayakawa and Hussain[43]

TABLE III. The maximum contour values of the coherent vorticity and Reynolds stresses for different yaw angles α.

α (deg)	Coherent values										
	$\tilde{\omega}_x^*$	$\tilde{\omega}_y^*$	$\tilde{\omega}_z^*$	$\tilde{u}^*$	$\tilde{v}^*$	$\tilde{w}^*$	$\tilde{u}^*\tilde{v}^*$	$\tilde{u}^*\tilde{w}^*$	$\tilde{v}^*\tilde{w}^*$	$\sqrt{\langle\omega_{xr}^2\rangle^*}$	$\sqrt{\langle\omega_{yr}^2\rangle^*}$
0	−0.15	−0.12	−0.8	0.12	−0.28	−0.04	−0.018	−0.005	−0.004	0.79	0.82
15	−0.15	−0.1	−0.8	0.14	−0.28	−0.04	−0.018	−0.006	−0.004	0.77	0.86
30	−0.25	−0.1	−0.6	0.10	−0.26	−0.06	−0.012	−0.007	−0.006	0.71	0.77
45	−0.25	−0.08	−0.4	0.08	−0.24	−0.08	−0.009	−0.009	−0.004	0.63	0.69

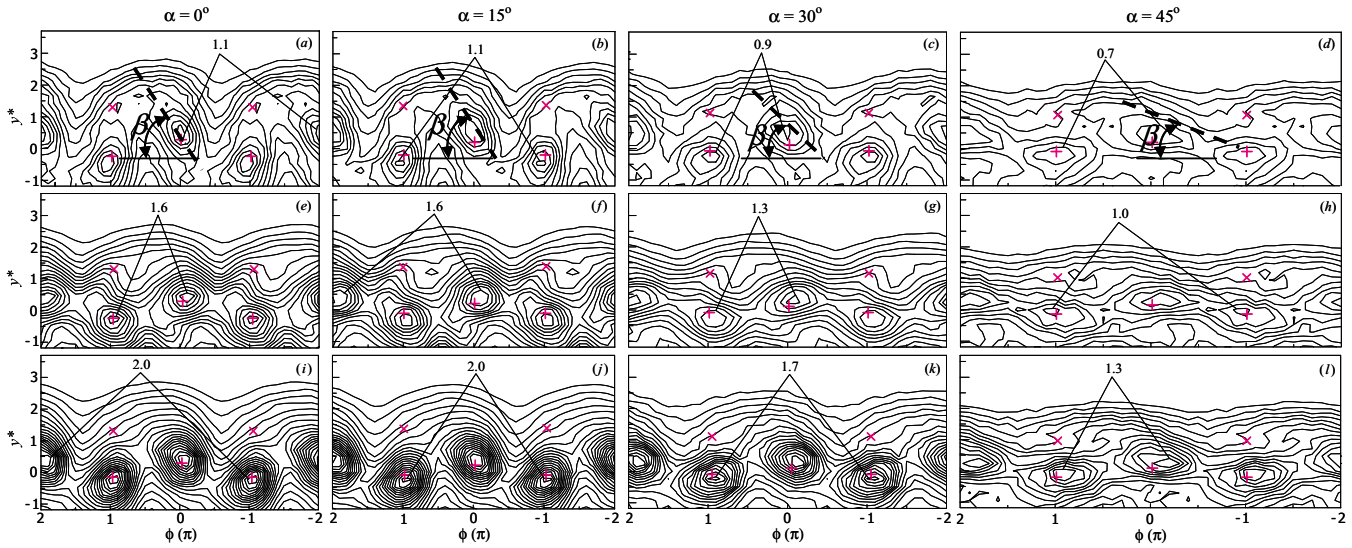

FIG. 9. (Color online) Phase-averaged incoherent vorticity contours at different α. [(a)–(d)] $\langle\omega_{xr}^2\rangle^*$; [(e)–(h)] $\langle\omega_{yr}^2\rangle^*$; [(i)–(l)] $\langle\omega_{zr}^2\rangle^*$. Center and saddle points are marked by plus and cross, respectively. The thick dashed line represents the stretching direction of the contours in $\langle\omega_{xr}^2\rangle^*$ and β is the angle of the stretching with respect to x-direction. Contour interval=0.1.

that the strength of the riblike structures in the cylinder wake is about the same as that of the spanwise structures, even in the yawed cylinder wake.

E. Topology of Reynolds stresses

The phase-averaged velocity components u, v, and w for different yaw angles are shown in Fig. 10. The $\tilde{u}^*$ contours [Figs. 10(a)–10(d)] are symmetric about y-axis and antisymmetric about the x-axis. The maximum concentration occurs at about $y/d=0.75$. The maximum value at $\alpha=0°$ agrees well with those reported previously in cylinder wake of a cross flow.[29,44] When α is increased to 15°, there is no apparent change in $\tilde{u}^*$, which is consistent with the trend revealed by the rms values of u.[39] When α is further increased to 30°, the maximum value of $\tilde{u}^*$ decreases by about 20%, and the range of the vortices also reduces, changing from $y^*=3.0$ at $\alpha=0°$ and 15° to about $y^*=2.7$ at $\alpha=30°$. The decreasing in the maximum $\tilde{u}^*$ concentration becomes more apparent at $\alpha=45°$ with a reduction in the wake range to $y^*=2.5$. This trend of $\tilde{u}^*$ indicates a reduction in the vortex shedding strength with the increase in α in a yawed cylinder wake. The $\tilde{v}^*$ contours [Figs. 10(e)–10(h)] are antisymmetric about $\phi=0$. The maximum value occurs at the centerline located in the alleyways between adjacent and opposite-signed spanwise vorticity contours. The maximum concentration of $\tilde{v}^*$ occurring at $\alpha=0°$ agrees well with those published previously.[29,44] With the increase in α to 30°, the maximum contour of $\tilde{v}^*$ decreases by about 7%. When α is further increased to 45°, the maximum value of $\tilde{v}^*$ reduces to 0.24, which is about 14% lower than that for $\alpha=0°$. These results indicate that with the increase in α, the intensity of the vortices decreases, which is consistent with that revealed by the vorticity contours (Fig. 7). The magnitude of $\tilde{v}^*$ is more than two times larger than that of $\tilde{u}^*$, indicating that the coherent structures contribute more to v than to u component, especially at large yaw angles.

In contrast to the coherent contours of $\tilde{u}^*$ and $\tilde{v}^*$, the magnitudes of $\tilde{w}^*$ contours [Figs. 10(i)–10(l)] are much smaller, indicating that the coherent structures contribute much less to w than that to the other two velocity compo-

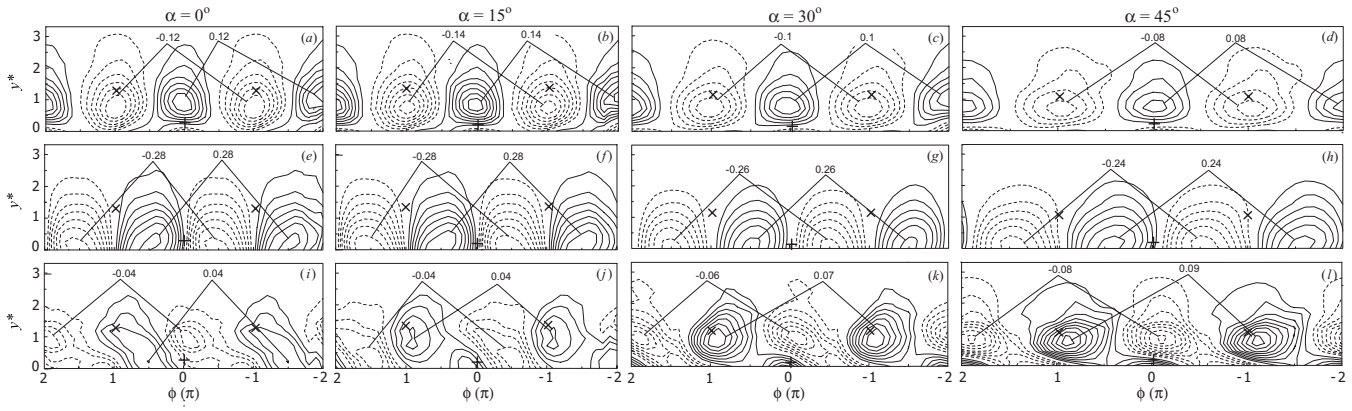

FIG. 10. Phase-averaged velocities at different α. [(a)–(d)] $\tilde{u}^*$; [(e)–(h)] $\tilde{v}^*$; [(i)–(l)] $\tilde{w}^*$. Center and saddle points are marked by plus and cross, respectively. [(a)–(d)] Contour interval=0.02; [(e)–(h)] 0.04; [(i)–(l)] 0.01.

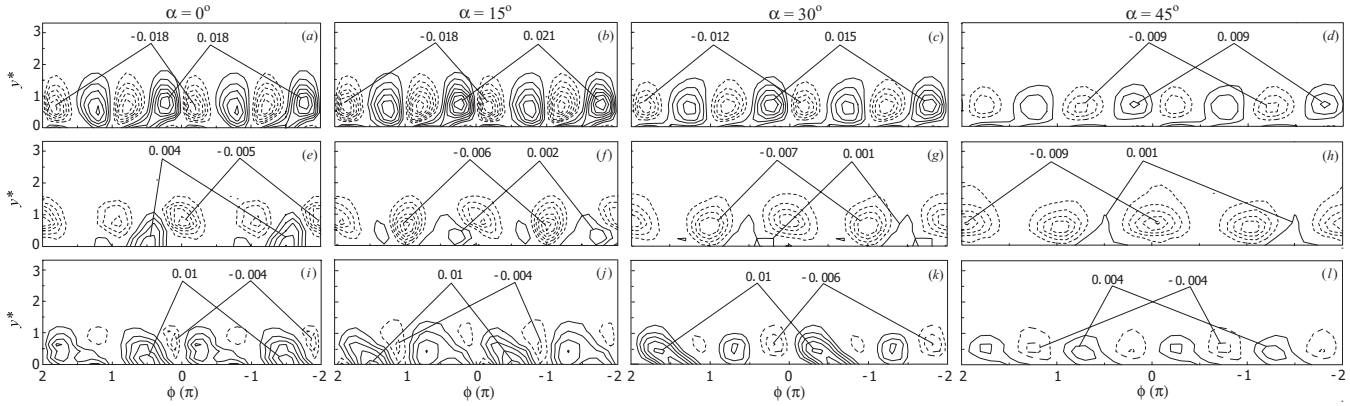

FIG. 11. Phase-averaged Reynolds shear stresses at different α. [(a)–(d)] $\tilde{u}^*\tilde{v}^*$; [(e)–(h)] $\tilde{u}^*\tilde{w}^*$; [(i)–(l)] $\tilde{v}^*\tilde{w}^*$. Center and saddle points are marked by plus and cross, respectively. [(a)–(d)] Contour interval=0.003; [(e) and (f)] 0.001; [(g)–(l)] 0.002.

nents. This result is consistent with the quasi-two-dimensional flow, especially when $\alpha \leq 15°$. Over this range of angles, the $\tilde{w}^*$ contours show much less regular patterns than that at higher α. When α is increased further, the organized patterns of $\tilde{w}^*$ become more apparent, with the maximum concentration being increased by about 50% at $\alpha=30°$ and by 100% at $\alpha=45°$ compared with that at $\alpha=0°$. At $\alpha=45°$, the maximum contours of $\tilde{u}^*$ and $\tilde{w}^*$ are comparable. The $\tilde{w}^*$ contours are antisymmetric about $y^*=0$ with the maximum concentration occurring at $y/d=\pm 0.75$. These results indicate that with the increase in α, secondary axial organized structures may be generated.[13,15,41,45] These structures may impair the quasi-two-dimensional structures and enhance the three dimensionality of the flow. This result is consistent with that shown by the increase in the spanwise mean velocity $\bar{W}$ and the increase in the autocorrelation coefficient of the spanwise velocity fluctuations for large values of α.[39] The maximum contour values of the coherent phase-averaged velocity components u, v, and w are also summarized in Table III.

The phase-averaged Reynolds shear stresses $\tilde{u}^*\tilde{v}^*$, $\tilde{u}^*\tilde{w}^*$, and $\tilde{v}^*\tilde{w}^*$ for different α are shown in Fig. 11. The $\tilde{u}^*\tilde{v}^*$ contours display a clover-leaf pattern about the vortex center, which is the result of the coherent velocity field associated with the vortical motion in a reference frame translating at U_c.[29] They are both antisymmetric about $\phi=0$ and about $y^*=0$, which implies that the distribution of $\overline{uv}$ should pass the origin of the coordinate system due to the cancellation of positive and negative $\tilde{u}^*\tilde{v}^*$. The maximum value of $\tilde{u}^*\tilde{v}^*$ contours does not change when α is increased from 0° to 15°. However, when α is increased to 30°, the $\tilde{u}^*\tilde{v}^*$ contours decrease by about 40%. When α is further increased to 45°, the wake region shrinks and the maximum contour value decreases significantly by 50%. This result is consistent with that given by Zhou *et al.*,[39] who showed that with the increase in α, the spanwise vortex shedding weakens. The contours of $\tilde{u}^*\tilde{w}^*$ also reveal apparent organized patterns (the negative contours in the upper part of the wake), although with much lower maximum concentration compared with that of $\tilde{u}^*\tilde{v}^*$. With the increase in α, the maximum concentration of $\tilde{u}^*\tilde{w}^*$ increases gradually, and at $\alpha=45°$, it is increased by 80% compared with that at $\alpha=0°$. This result confirms the generation of the secondary vortex induced by the spanwise mean velocity shear $\partial\bar{W}/\partial y$.[39] The $\tilde{v}^*\tilde{w}^*$-contours display an alternately signed pattern similar to those of $\tilde{u}^*\tilde{v}^*$, although there is a considerable phase difference between them [Figs. 11(c), 11(d), 11(k), and 11(l)], which increases with increasing α, reaching about π at $\alpha=45°$. This is expected since the $\tilde{u}^*$- and $\tilde{w}^*$-contours are similar in pattern but opposite in sign, i.e., with a phase difference, which grows with α [Figs. 10(c), 10(d), 10(k), and 10(l)]. The maximum magnitude of $\tilde{v}^*\tilde{w}^*$ at $\alpha=0°$ is much smaller than that of $\tilde{u}^*\tilde{v}^*$ but comparable to that of $\tilde{u}^*\tilde{w}^*$, and is furthermore essentially independent of α, probably because with increasing α, the maximum magnitude reduces in $\tilde{v}^*$ but increases in $\tilde{w}^*$ (Fig. 10). The maximum magnitudes of $\tilde{u}^*\tilde{v}^*$, $\tilde{u}^*\tilde{w}^*$, and $\tilde{v}^*\tilde{w}^*$ for different α are summarized in Table III.

V. COHERENT AND INCOHERENT CONTRIBUTIONS TO VELOCITY AND VORTICITY VARIANCES

After the coherent components of the velocity and vorticity signals are extracted, the coherent contributions to Reynolds stresses and vorticity variances can be obtained in terms of their structural average. The coherent and incoherent contributions of the velocity variances for different yaw angles are shown in Fig. 12. The time averaged values are also included. For the u component [Figs. 12(a)–12(d)], the coherent contribution displays a peak at around $y^*=0.75$. Due to the symmetry of the flow, another peak in the distribution is expected at $y^*=-0.75$. This distribution results in double peaks on the u velocity variance across the wake, which is consistent with Figs. 10(a)–10(d). The main contribution to the velocity variance is from the incoherent component, especially at the wake centerline, where the coherent component is nearly zero. For $\alpha=0°$, the coherent component $\overline{\tilde{u}^{*2}}$ is about 50% of the incoherent one $\overline{\tilde{u}_r^{*2}}$ at $y^*=0.75$, which is consistent with that reported previously.[29] This value is comparable to those for $\alpha=15°$ (60%) and 30° (57%). When $\alpha=45°$, the coherent component reduces to 30% of the incoherent one, suggesting that with the increase

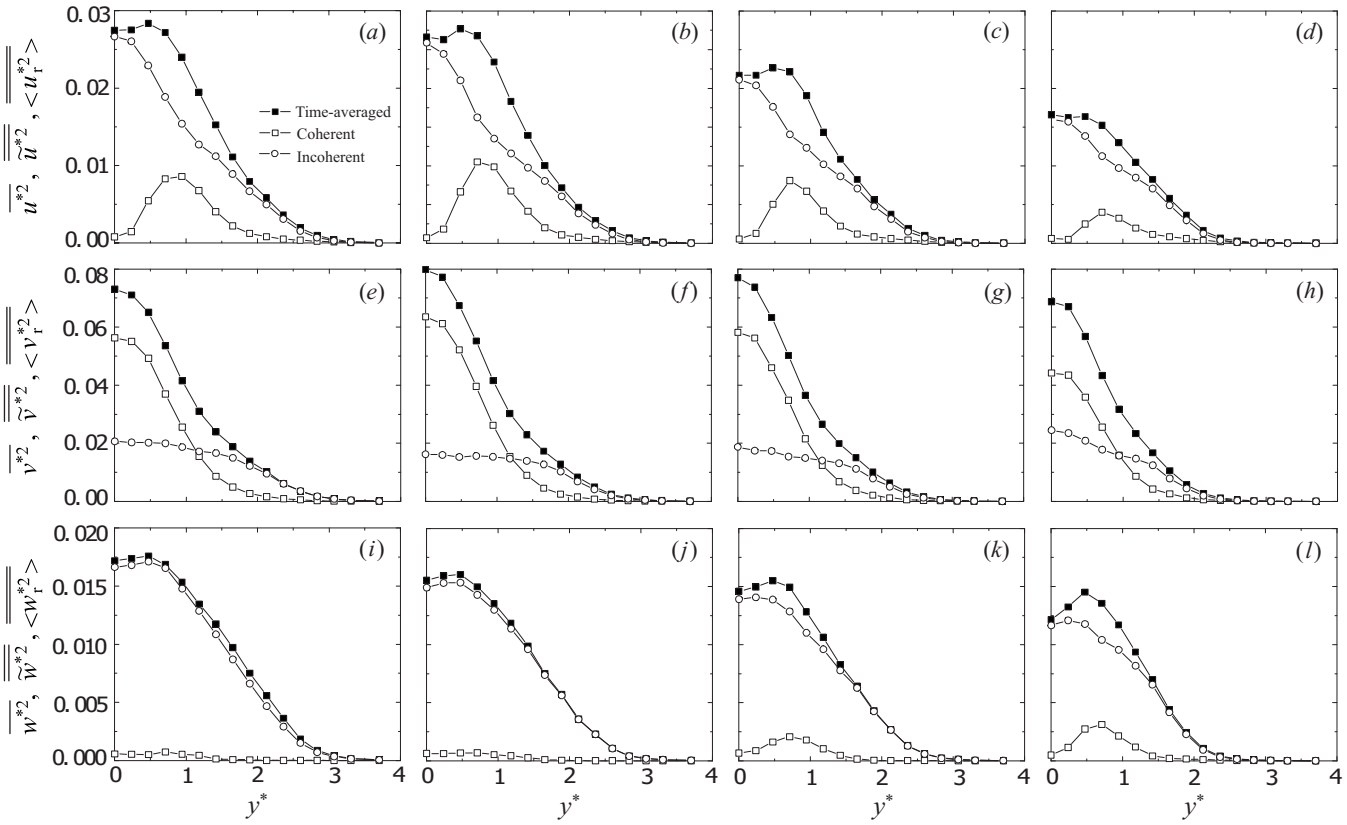

FIG. 12. Time-averaged Reynolds normal stresses and their coherent and incoherent contributions at different α. [(a), (e), and (i)] $\alpha=0°$; [(b), (f), and (j)] $\alpha=15°$; [(c), (g), and (k)] $\alpha=30°$; [(d), (h), and (l)] $\alpha=45°$.

in α, the large-scale organized structures become less intensified, which may be related with the breakdown of the large-scale structures. This result may also be related with the increase in the spanwise velocity component, which is generally regarded as the deterioration of the two dimensionality of the flow.[39,41] It is apparent that the coherent structures contribute to the v velocity component more significantly than to the other two velocity components at all yaw angles [Figs. 12(e)–12(h)]. The coherent contribution to $\overline{v^{*2}}$ for all yaw angles dominates in the central part of the wake ($-1 \leq y^* \leq 1$). When α is increased, the coherent contribution to $\overline{v^{*2}}$ decreases while the incoherent contribution increases. For example, at $\alpha=45°$, the ratio of the coherent component to the incoherent component is about 1.8 at the wake centerline. This ratio is smaller than those at other yaw angles on the wake centerline, which are 2.9, 3.9, and 2.9 for $\alpha=0°$, 15°, and 30°, respectively. As the v velocity component is sensitive to the large organized structures, this result indicates that with the increase in α, the large-scale organized structures break down and become less intensified as compared with that at $\alpha=0°$. The coherent contributions to $\overline{w^{*2}}$ are very small at $\alpha=0°$ and 15° [Figs. 12(i)–12(l)]. Nearly 96% contribution to the time averaged $\overline{w^{*2}}$ is from the incoherent structures. This result is consistent with the quasi-two-dimensionality of the wake flow for small yaw angles. When α increases to 30° and 45°, the coherent contribution to $\overline{w^{*2}}$ increases, changing to 15% and 22%, respectively. The coherent component $\overline{\tilde{w}^{*2}}$ also displays a peak at about $y^*=0.75$. This peak location is consistent with that revealed by $\overline{\tilde{u}^{*2}}$ [Figs. 12(a)–12(d)] and the mean velocity gradients (Fig. 5).

The coherent contributions to the vorticity variances for different α are shown in Fig. 13. At $\alpha=0°$ [Fig. 13(a)], the coherent contribution to the longitudinal vorticity component is essentially negligible (less than 1%). This result is consistent with that shown by Zhou *et al.*[38] and is also consistent with that revealed by the longitudinal vorticity contours [Fig. 7(a)]. As pointed out earlier, the detection of the organized structures is based on the spanwise structures, which may result in negligibly small values of $\tilde{\omega}_x^*$ due to the cancellation of the opposite-signed vorticity in phase averaging. It can still be seen that with the increase in α, the coherent contribution to ω_x increases, changing from about 1% at $\alpha=0°$ to 6% at $\alpha=45°$. This result is in agreement with the phase-averaged longitudinal vorticity contours [Fig. 5(a)], which shows that with the increase in α, the maximum longitudinal vorticity concentration also increases. The coherent contribution to the lateral vorticity variance $\overline{\tilde{\omega}_y^2}$ is one order smaller than that for ω_x [Fig. 13(b)]. The largest coherent contribution is to the spanwise vorticity $\overline{\tilde{\omega}_z^2}$ [Fig. 13(c)], which is about 24% on the centerline. With the increase in α, the coherent contribution to ω_z decreases. This result indicates that with the increase in α, the intensity of the spanwise vorticity components decreases, resulting in a reduction in the coherent vorticity variance. It seems that the increase in

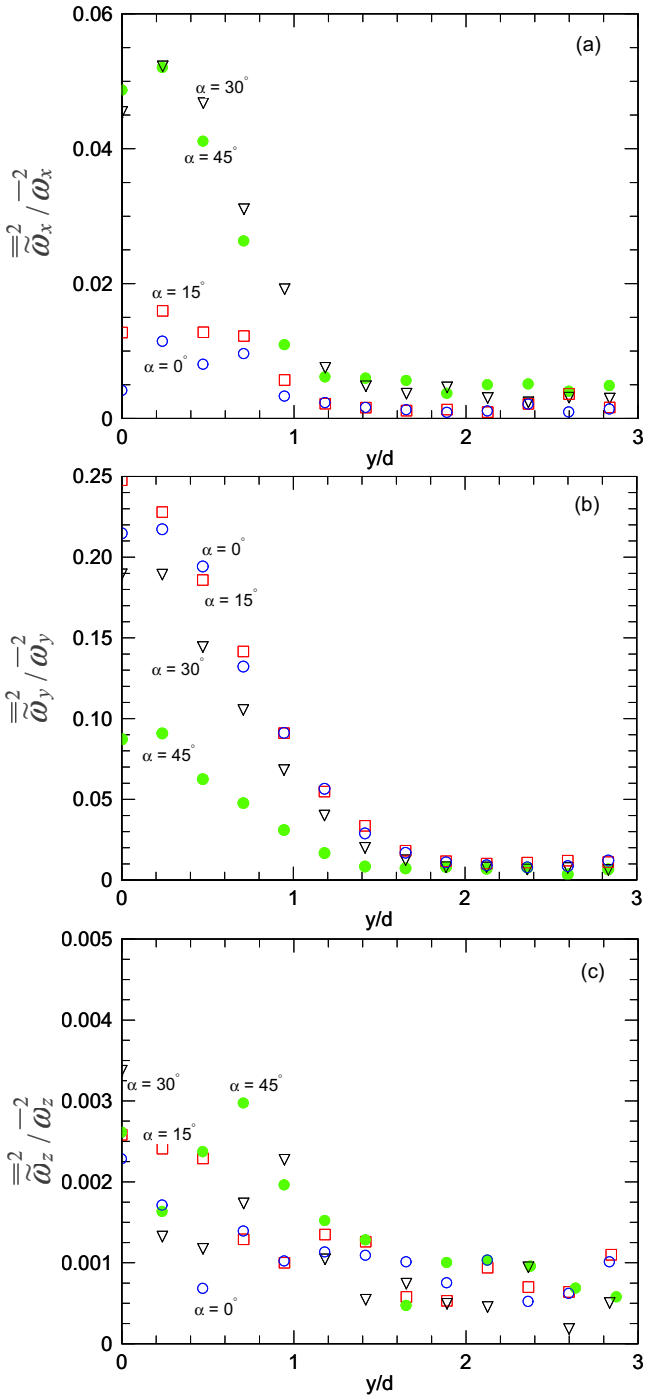

FIG. 13. (Color online) Lateral distribution of coherent contributions to vorticity variances. (a) $\overline{\tilde{\omega}_x^2}/\overline{\omega_x^2}$; (b) $\overline{\tilde{\omega}_y^2}/\overline{\omega_y^2}$; (c) $\overline{\tilde{\omega}_z^2}/\overline{\omega_z^2}$.

the streamwise vorticity is at the expense of the reduction in the spanwise vorticity, supporting the result of Mansy *et al.*[40] The present results shown in Fig. 13 indicate that vorticity mostly resides in relatively smaller-scale structures. Note the fact that the coherent contribution is calculated based on the detection of the spanwise vortical structures, the contribution from the longitudinal structures to the vorticity variances may not be taken into account in the coherent variances $\overline{\tilde{\beta}^2}$, rather this contribution may be included in the incoherent variances $\langle\overline{\beta_r^2}\rangle$.

VI. CONCLUSIONS

An eight-hot wire vorticity probe has been used to measure simultaneously the 3D velocity and vorticity components in the intermediate wake ($x/d=10$) of a stationary circular cylinder at a yaw angle in the range of 0°–45°. The phase-averaged technique is used to analyze the large-scale organized vortex structures of the wakes. The main results are summarized as follows.

(1) The instantaneous vorticity signals of ω_x, ω_y, and ω_z are comparable in magnitude and show relatively large-scale fluctuations near the spanwise vortex centers. When α increases, the vorticity signals exhibit higher intermittency.

(2) There is an apparent peak on the spanwise vorticity spectrum, which corresponds to the shedding frequency of the Kármán vortex. When α is small, the peak is narrow and sharp. When α is increased to 45°, the peak region of the spanwise vorticity spectra is enlarged and the peak height of ϕ_{ω_z} is reduced, while that of ϕ_{ω_x} is increased, indicating a dispersion of the turbulent energy over the vortex shedding frequency, as well as the enhancement of the three dimensionality of the flow at large yaw angles.

(3) Based on the phase-averaging technique, the coherent contours of the three vorticity components show apparent Kármán vortex shedding phenomena. At $\alpha=0°$, the maximum concentration of the spanwise vorticity component is about six times of the longitudinal and transverse ones. For $\alpha\leq 15°$, the maximum concentration of the three vorticity components does not depend on α. However, when α increases to 45°, the maximum coherent concentrations of the transverse and spanwise vorticity components at the vortex center decrease by about 33% and 50%, respectively, while the contours of the longitudinal vortices become more organized with the maximum concentration being increased by 70%. This result indicates the generation of the secondary axial vortices, which is consistent with that found by Matsumoto *et al.*[15] It also supports the argument of Mansy *et al.*[40] that the increase in the streamwise circulations is at the expense of the primary spanwise vortex circulation. The maximum coherent concentrations of the streamwise and spanwise vorticity components at the vortex center are comparable in magnitude at $\alpha=45°$. These results indicate that the three dimensionality of the wake flow has been enhanced significantly when α is increased to 45°.

(4) The incoherent vorticity contours $\langle\omega_{xr}^2\rangle^*$ are stretched along an axis inclining to the x-axis at an angle β in the range of 60°–25° when α is changed from 0° to 45°. The magnitudes of $\sqrt{\langle\omega_{xr}^2\rangle^*}$ and $\sqrt{\langle\omega_{yr}^2\rangle^*}$ (Fig. 9) through the saddle point are comparable to the maximum magnitude of the coherent spanwise vorticity component $\tilde{\omega}_z^*$ at all cylinder yaw angles (Fig. 7). This result supports the speculation of Hayakawa and Hussain[43] that the strength of the riblike structures in the cylinder wake is about the same as that of the spanwise structures, even in the yawed cylinder wakes.

(5) The contours of the three velocity components exhibit apparent vortex patterns at all yaw angles. With the increase in α, the maximum concentrations of u and v contours decrease, while those of $\tilde{w}^*$ become more apparent with the maximum concentration being increased by about 50% at $\alpha=30°$ and by 100% at $\alpha=45°$ compared with that at $\alpha=0°$. Correspondingly, the coherent contributions to the velocity variances $\langle u^2\rangle$ and $\langle v^2\rangle$ decrease while that to $\langle w^2\rangle$ increases.

(6) The coherent contribution to $\overline{\overline{\tilde{\omega}_x^2}}$ at $\alpha=0°$ is negligible. With the increase in α, the coherent contribution to $\overline{\overline{\tilde{\omega}_x^2}}$ increases slightly. In contrast, the coherent contributions to $\overline{\overline{\tilde{\omega}_y^2}}$ and $\overline{\overline{\tilde{\omega}_z^2}}$ decrease with increasing α. These results suggest that the strength of the Kármán vortex shed from the yawed cylinder decreases and the three dimensionality of the flow is enhanced when α is increased.

[1] M. Provansal, "Bénard–von Kármán instability: Transient and forced regimes," J. Fluid Mech. **182**, 1 (1987).
[2] C. H. K. Williamson, "Three-dimensional wake transition," J. Fluid Mech. **328**, 345 (1996).
[3] C. Norberg, "An experimental investigation of the flow around a circular cylinder: Influence of aspect ratio," J. Fluid Mech. **258**, 287 (1994).
[4] C. H. K. Williamson, "Vortex dynamics in the cylinder wake," Annu. Rev. Fluid Mech. **28**, 477 (1996).
[5] C. H. K. Williamson, "The existence of two stages in the transition to three-dimensionality of a cylinder wake," Phys. Fluids **31**, 3165 (1988).
[6] C. H. K. Williamson and A. Roshko, "Measurements of base pressure in the wake of a cylinder at low Reynolds numbers," Z. Flugwiss. Weltraumforsch. **14**, 38 (1990).
[7] C. H. K. Williamson, "The natural and forced formation of spot-like 'vortex dislocations' in the transition wake," J. Fluid Mech. **243**, 393 (1992).
[8] T. Leweke and M. Provansal, "The flow behind rings: Bluff body wakes without end effect," J. Fluid Mech. **288**, 265 (1995).
[9] M. C. Thompson, K. Hourigan, K. Ryan, and G. J. Sheard, "Wake transition of two-dimensional cylinders and axisymmetric bluff bodies," J. Fluids Struct. **22**, 793 (2006).
[10] R. D. Henderson and D. Barkley, "Secondary instability in the wake of a circular cylinder," Phys. Fluids **8**, 1683 (1996).
[11] A. Prasad and C. H. K. Williamson, "Three-dimensional effects on turbulent bluff-body wakes," J. Fluid Mech. **343**, 235 (1997).
[12] C. Norberg, "Pressure forces on a circular cylinder in cross-flow," *UITAM Symposium Bluff-Body Wake, Dynamics and Instabilities*, Göttingen, Germany (Springer-Verlag, Berlin, 1992).
[13] S. Szepessy and P. W. Bearman, "Aspect ratio and end plate effects on vortex shedding from a circular cylinder," J. Fluid Mech. **234**, 191 (1992).
[14] M. Matsumoto, N. Shiraishi, and H. Shirato, "Rain-wind induced vibration of cables of cable-stayed bridges," J. Wind. Eng. Ind. Aerodyn. **43**, 2011 (1992).
[15] M. Matsumoto, T. Yagi, Y. Shigemura, and D. Tsushima, "Vortex-induced cable vibration of cable-stayed bridges at high reduced wind velocity," J. Wind. Eng. Ind. Aerodyn. **89**, 633 (2001).
[16] M. M. Alam and Y. Zhou, "Turbulent wake of an inclined cylinder with water running," J. Fluid Mech. **589**, 261 (2007).
[17] R. King, "Vortex excited oscillations of yawed circular cylinders," ASME Trans. J. Fluids Eng. **99**, 495 (1977).
[18] S. E. Ramberg, "The effect of yaw and finite length upon the vortex wakes of stationary and vibrating circular cylinders," J. Fluid Mech. **128**, 81 (1983).
[19] A. Kozakiewicz, J. Fredsøe, and B. M. Sumer, "Forces on pipelines in oblique attack: Steady current and waves," Proceedings of the Fifth International Offshore and Polar Engineering Conference, The Hague, The Netherlands, 11–16 June 1995.
[20] D. Lucor and G. E. Karniadakis, "Effects of oblique inflow in vortex-induced vibrations," Flow, Turbul. Combust. **71**, 375 (2003).
[21] A. Thakur, X. Liu, and J. S. Marshall, "Wake flow of single and multiple yawed cylinders," ASME Trans. J. Fluids Eng. **126**, 861 (2004).
[22] C. W. Van Atta, "Experiments on vortex shedding from yawed circular cylinders," AIAA J. **6**, 931 (1968).
[23] K. Chiba and A. Horikawa, "Numerical solution for the flow of viscoelastic fluids around an inclined circular cylinder," Rheol. Acta **26**, 243 (1987).
[24] J. S. Marshall, "Wake dynamic of a yawed cylinder," ASME Trans. J. Fluids Eng. **125**, 97 (2003).
[25] M. Zhao, L. Cheng, and T. Zhou, "Direct numerical simulation of three-dimensional flow past a yawed circular cylinder of infinite length," J. Fluids Struct. **25**, 831 (2009).
[26] D. Yeo and N. P. Jones, "Investigation on 3-D characteristics of flow around a yawed and inclined circular cylinder," J. Wind. Eng. Ind. Aerodyn. **96**, 1947 (2008).
[27] H. Tennekes and J. L. Lumley, *A First Course in Turbulence* (MIT, Cambridge, MA, 1972).
[28] M. Kiya and M. Matsumura, "Turbulence structure in intermediate wake of a circular cylinder," Bull. JSME **28**, 2617 (1985).
[29] Y. Zhou, H. J. Zhang, and M. W. Yiu, "The turbulent wake of two side-by-side circular cylinders," J. Fluid Mech. **458**, 303 (2002).
[30] H. Sakamoto, H. Haniu, and Y. Obata, "Fluctuating forces acting on two prisms in a tandem arrangement," J. Wind. Eng. Ind. Aerodyn. **26**, 85 (1987).
[31] J. M. Wallace and J. F. Foss, "The measurement of vorticity in turbulent flows," Annu. Rev. Fluid Mech. **27**, 469 (1995).
[32] S. J. Kline and F. A. McClintock, "Describing uncertainties in single experiments," Mech. Eng. **75**, 3 (1953).
[33] R. J. Moffat, "Using uncertainty analysis in the planning of an experiment," ASME Trans. J. Fluids Eng. **107**, 173 (1985).
[34] R. J. Moffat, "Describing the uncertainties in experimental results," Exp. Therm. Fluid Sci. **1**, 3 (1988).
[35] R. A. Antonia, T. Zhou, and Y. Zhu, "Three-component vorticity measurements in a turbulent grid flow," J. Fluid Mech. **374**, 29 (1998).
[36] Y. Zhou and R. A. Antonia, "A study of turbulent vortices in the near wake of a cylinder," J. Fluid Mech. **253**, 643 (1993).
[37] S. Kida and Y. Murakami, "Statistics of velocity gradients in turbulence at moderate Reynolds numbers," Fluid Dyn. Res. **4**, 347 (1989).
[38] T. Zhou, Y. Zhou, M. W. Yiu, and L. P. Chua, "Three-dimensional vorticity in a turbulent cylinder wake," Exp. Fluids **35**, 459 (2003).
[39] T. Zhou, S. F. M. Razali, Y. Zhou, L. P. Chua, and L. Cheng, "Dependence of the wake on inclination of a stationary cylinder," Exp. Fluids **46**, 1125 (2009).
[40] H. Mansy, P.-M. Yang, and D. R. Williams, "Quantitative measurements of three-dimensional structures in the wake of a circular cylinder," J. Fluid Mech. **270**, 277 (1994).
[41] M. Hammache and M. Gharib, "An experimental study of the parallel and oblique vortex shedding from circular cylinders," J. Fluid Mech. **232**, 567 (1991).
[42] A. K. M. F. Hussain, "Coherent structures and turbulence," J. Fluid Mech. **173**, 303 (1986).
[43] M. Hayakawa and F. Hussain, "Three-dimensionality of organized structures in a plane turbulent wake," J. Fluid Mech. **206**, 375 (1989).
[44] M. Matsumura and R. A. Antonia, "Momentum and heat transport in the turbulent intermediate wake of a circular cylinder," J. Fluid Mech. **250**, 651 (1993).
[45] C. Norberg, "Flow around a circular cylinder: Aspects of fluctuating lift," J. Fluids Struct. **15**, 459 (2001).